Correlative analysis of advanced microscopy techniques for metallography and corrosion microstructures of bronze phoenician coins

Martina Bernabale [a,b], Flavio Cognigni [c], Silvia Contessi [d], Anacleto Proietti [b], Chiara Mancini [b], Federica Spagnoli [e], Marco Rossi [b,f], Caterina De Vito [a,*]

[a] Department of Earth Sciences, Sapienza University of Rome, P.le Aldo Moro 5, 00185 Rome, Italy
[b] Department of Basic and Applied Sciences for Engineering (SBAI), Sapienza University of Rome, Via Antonio Scarpa 14, 00161 Rome, Italy
[c] Carl Zeiss S.p.A, Research Microscopy Solutions, Via Varesina, 162, 20156 Milan, Italy
[d] Department of Medical and Surgical Sciences (DIMEC), Alma Mater Studiorum-University of Bologna, Via P. Palagi 9, 40138 Bologna, Italy
[e] Department Italian Institute of Oriental Studies - ISO, Sapienza University of Rome, Circonvallazione Tiburtina 4, 00185 Rome, Italy
[f] Research Center on Nanotechnologies Applied to Engineering (CNIS), Sapienza University of Rome, P.le Aldo Moro 5, 00185 Rome, Italy

ABSTRACT

Correlative microscopy stands out for its ability to concurrently acquire and analyze various data types in a multimodal and multiscale environment, enabling precise localization of specific areas within samples and enhancing the accuracy and relevance of analyses. This approach showed promise in revealing the metallurgical history of ancient coins. This article focused on composition, microstructure, and manufacturing process of Phoenician-Punic copper-based alloy coins (5th–4th century BCE). The four coins studied by correlative light and electron microscopy, μ-Raman spectroscopy, and X-ray Microscopy exhibited notable differences in elemental composition and microstructures. These variations are attributed to their origin from casting, followed by striking, and subsequent recrystallization due to a more intricate corrosion process.

1. Introduction

Archaeometric and diagnostic studies on ancient numismatic materials using traditional analytical techniques have provided important aspectsrelated to minting technologies, economic trends, political interactions, and numismatic and cultural exchanges between ancient states and groups [1]. For instance, Light Microscopy (LM) and Scanning Electron Microscopy (SEM) are commonly employed to investigate the surface morphology of coins, while X-ray Fluorescence (XRF), Atomic Absorption Spectroscopy (AAS), Inductively Coupled Plasma (ICP) Analysis, and X-ray Photoelectron Spectroscopy (XPS) are used to analyze their chemical composition and infer the metals used in their production; X-Ray Diffraction (XRD) and μ-Raman spectroscopy are generally used to identifying the mineralogical composition of alteration products [2–11]. Additionally, the microstructural information about the inner core of the coins obtained by cutting-edge X-rays and neutron methods expands the possibilities of traditional studies of coins, providing new insight into coinage manufacturing andcoins degradation like internal corrosion tracks [12–15].

However, these single investigation techniques face several limitations leading to non-correlative imaging workflows where similar yet distinct samples or regions are imaged separately in each system. Moreover, this approach imposes inherent constraints regarding the visualization of the overall appearance of the artifact and the representativeness of the selected regions of interest (ROIs) compared to others. Consequently, this difficulty hinders the ability to establish connections between the microscopic characteristics identified in an ROI within the artifact as well as their relationship with its macroscopic features.

To address and overcome these limitations, it is of paramount importance to develop innovative multiscale and multimodal correlative microscopy workflows based on state-of-the-art hardware and software solutions [16–19]. Indeed, crucial morphological and compositional features are present at multiple length scales within the sample, generating the researchers' need to first obtain a macroscale overview of the specimen in a connected and multimodal environment opening the door to advanced analyses and considerations. This integration allows for the extraction of topographical, morphological, microstructural, and chemical properties contained in high-resolution imaging and their connection to a larger volume obtained from lower-resolution imaging,

---

thereby enhancing our understanding of the complex samples [20,21].

This research endeavors to achieve several critical objectives. It seeks to assess the degree of corrosion present on four Punic coins from Motya (Sicily, Italy) and elucidate its intricate connection with the chemical and physical characteristics of the coin alloys. Then, this study aims to provide comprehensive insights into the manufacturing techniques employed in the production of these coins. Moreover, a significant focus of our scientific contribution is the application of a repeatable methodological approach based on the specific combination and correlation of advanced microscopy techniques using ZEISS ZEN Connect software, which allows for the integration of 2D images acquired using different characterization tools. By merging information derived from diverse techniques, such as non-invasive methods and advanced three-dimensional microstructural investigations, we can construct a more holistic and accurate history of the corrosion processes these coins have undergone. This approach is particularly valuable when studying metals and their alloys, which exhibit significant heterogeneity, produced by the coexistence of multiple phases, segregation, or inclusions [22–25]. Certainly, the relatively rudimentary smelting technology used in ancient times has resulted in notable corrosion discrepancies among bronze cultural artifacts with distinct compositions. This poses a notable challenge in precisely controlling both the smelting temperature of the alloy and the chemical composition ratio in different areas of the artifacts. [26]. Hence, correlative analysis plays a pivotal role in the examination of the corrosion behavior and characteristics of bronze alloys.

Here we present a multiscale and multimodal correlative microscopy workflow by combining X-ray Microscopy (XRM), μ-Raman spectroscopy, Light Microscopy (LM), and Scanning Electron Microscopy (SEM) [27,28]. This integration is made possible by using a specially designed software tool, enabling the simultaneous examination of various microscopy images and data from the same ROIs within a sample in a unified context.

2. Archaeological context and materials

The ancient city of Motya, located on the island of San Pantaleo (Sicily, Italy), is one of the most important Phoenician colonies in the central Mediterranean area. On the island, several monetary artifacts have been found, dating back to a period ranging from the last quarter of the 5th century BCE to the first quarter of the 4th century BCE [29]. These discoveries were made during excavations conducted by the archaeological mission of Sapienza University, directed by L. Nigro, in Zone D during the campaigns undertaken between 2002 and 2004.

The coinage of Motya represents a significant reflection of the Hellenization process that took place during the 5th century, as well as the political and cultural dialogue between Motya and the Greek-Sicilian world [30]. This affected the dispersion and circulation of currency in the eastern part of Sicily and a broader Mediterranean context, involving the cities of Magna Graecia and Etruria. Therefore, the Punic coins of Motya are a crucial source of information for understanding the history of the ancient Phoenician-Punic civilization, their commercial activities, and their production techniques.

The analyzed coins (Table 1S, **Supplementary Materials**) appear to belong to the 'supra-regional' category of coins, characterized by generic Punic types featuring stereotypical images. In contrast to these 'regional' types, which are typically associated with Sicilian production, these coins generally depict a male head and a prancing horse, or a palm tree and a horse's head for the subsequent type. Both the horse, sometimes linked to the foundation myth of Carthage and a sun god, and the palm tree, symbolizing fertility and a pun on 'Phoenician,' are highly emblematic. These coin types were designed for interregional circulation, and standardized images facilitated trade.

The notable presence of regional and supra-regional Punic bronzes in Sicily after the mid-fourth century is directly linked to the island's economic resurgence following the treaty between Syracuse and Carthage in 339/8 BCE. The overall coin circulation pattern in Sicily

consists of a limited number of regional Sicilian types, with the majority of coinage comprised of supra-regional types. Most of these supra-regional coins were minted in Sicily, although some may have originated from either Sicily or Carthage, and few others were issued in Sardinia [31].

3. Experimental

Despite non-invasive XRM analyses were performed initially to guide sampling and identification of cross-sections, microstructural and chemical compositions by OM, SEM-EDS, and μ-Raman spectroscopy are first presented to understand the chemical composition and stratigraphy of the corrosion layers. Then, the XRM is correlated with the corrosion structures.

To perform correlative microstructural and chemical investigations by Light microscopy (LM) and Scanning Electron Microscopy (SEM) at ZEISS Technological Center of Reggio Emilia (Italy) a small fragment of each coin was cut and embedded in epoxy resin to produce cross sections. These cross sections were then polished with SiC abrasive papers (grades from 800 to 4000) and finished with diamond paste (up to 1 μm) to achieve perfectly polished surfaces.

Subsequently, the coins were examined through μ-Raman spectroscopy and individually scanned with ZEISS Xradia Versa 610 and at Sapienza Nanoscience & Nanotechnology Laboratories (SNN-Lab) of the Research Center on Nanotechnology Applied to Engineering (CNIS) of Sapienza University.

3.1. Light microscopy (LM)

LM observations were performed using a ZEISS Axio Imager (Carl Zeiss GmbH, Oberkochen, Germany) equipped with a motorized table, 20×, 50×, 100× objectives and coupled with an AxioCam 503 colour available at the Carl Zeiss S.p.A. - Quality Excellence Center, Reggio Emilia, Italy).

3.2. Scanning electron microscopy (SEM) and energy dispersive X-ray spectroscopy (EDX)

SEM and EDX investigations were performed using a ZEISS EVO 15 (Carl Zeiss GmbH, Oberkochen, Germany) equipped with Ultim Max 65 mm^2 (Oxford Instruments, Abingdon-on-Thames, United Kingdom) EDX probe available at the Carl Zeiss S.p.A. - Quality Excellence Center (Reggio Emilia, Italy). SEM images and EDX spectra/maps were acquired using the following parameters: acceleration voltage 25 kV, probe current 300 pA, aperture size 30 ɥm, WD 8.5 mm.

3.3. Correlative light and electron microscopy (CLEM)

LM, SEM and EDX experiments were performed in a correlative microscopy environment provided by ZEN Connect software (Carl Zeiss GmbH, Oberkochen, Germany).

3.4. μ-Raman spectroscopy

Raman spectra were obtained using an inViaTM confocal Raman spectrometer (Renishaw) with a focal length of 250 *mm*. Analyses were performed at room temperature in the spectral range 180–1940 cm^{-1}, excluding certain ranges that gave non-informative data. A 1800 *l/mm* holographic grating scattered the signal, which was then collected by a Peltier-cooled CCD detector. The samples were excited using two different lasers: a Nd:YAG (from Renishaw) continuous-wave diode-pumped solid-state laser with a wavelength of 532.1 *nm* and an output power of 50 *mW* and a HeNe (from Renishaw) continuous-wave diode-pumped solid-state laser with a wavelength of 632.816 *nm* and an output power of 17.5 *mW*.

The laser beam was focused onto the sample using a short working-

distance 100× N-Plan objective (NA = 0.88, from Leica Microsystems). The acquired Raman spectra were processed using WiRE™ 4.4 software for normalization, fitting procedures, and peak position determination. Peak positions were calibrated using both internal and external silicon references.

Measurements were performed using both green (532 nm) and red (633 nm) lasers, with power settings ranging from 10 % to 50 % for the green laser (Fig. 5, spectra b,c,d,e,f) and 100 % for the red laser (Fig. 5, spectrum a). Each measurement consisted of an exposure time of 1 s and an average of 30 accumulations.

3.5. X-ray microscopy and dataset reconstruction

X-ray Microscopy (XRM) experiments were performed using a ZEISS Xradia Versa 610 (Carl Zeiss X-ray microscopy, Dublin, CA, USA) available at the Research Center on Nanotechnology Applied to Engineering of Sapienza University of Rome (CNIS), which is part of the Open Infrastructure for Advanced TOmography and Microscopies (ATOM). XRM allowed the multiscale acquisition of a set of projection images of samples at different viewing angles, from −180 to +180, achieved by rotating the sample. The set of projections was fed into the cone-beam Feldkamp-Davis-Kress (FDK) algorithm to obtain the 3D model of each specimen. Low- and high-resolution XRM was performed setting a camera binning 2 and adopting the parameters reported in Table 1.

3.6. 3D modeling and post-processing

XRM 3D datasets were analyzed using Dragonfly Pro (*V.* 2022.1 Build 1259, Object Research Systems, Montreal, Quebec, Canada) software. High-resolution XRM datasets were filtered using a Non-local Means (NLM) filter (Kernel Size 9; Smoothing 0.5) to reduce the noise while preserving sharp edges.

4. Results

4.1. Correlative light and electron microscopy (CLEM) for metallography and corrosion microstructure investigation

Correlative light and electron microscopy (CLEM) allows for a multiscale and multimodal integration of 2D datasets obtained from various characterization tools, such as LM, SEM and Energy Dispersive X-ray Spectroscopy (EDX). By harnessing advanced correlative microscopy softwares, like ZEISS ZEN Connect, it becomes possible to precisely target and overlay specific regions or features within the cross-section of the coin while preserving the general overview of the specimen.

Fig. 1a reveals that coin MO 89 BIII 43/3 is a cast copper alloy with a complex corroded dendritic microstructure. These dendrites likely formed during the cooling process after casting and are indicative of a tin-copper solid solution in the bronze alloy, where copper serves as the solvent and tin as the solute. The dendritic structure is a commonly observed microstructure resulting from casting and cooling processes in several ancient bronze objects. Indeed, dendrites form due to the

discrepancy in melting points between copper and tin, which are 1083 °C and 232 °C, respectively.

The metal is inhomogeneous and consists mostly of cored and corroded dendrites of composition 1, 2 and 3 (analyses in Fig. 1, Table 2). The end composition of α-Cu solid solution, which solidified first and corresponds to the bright gold dendrites by LM, is mostly copper (97 wt%), containing small amounts of Sn (3 wt%). Optical bright-field observations of the sample further revealed that in certain areas of the dendrites, the composition of the α-Cu dendrites changes (composition 1). These regions show a composition of about 92 % Cu, 4 % Sn, and 4 % Cl. This phenomenon marks the initial stage of the corrosion mechanism of the alpha phase and can be explained by the pseudomorphic substitution of the former metallic structure with Cl-phases. Compositions 1 and 2 represent the onset of dendritic crystallization, whereas composition 3 containing ca 66 wt% of Cu and ca. 5 wt % of Sn, with a significant amount of Cl (29 wt%) marks its termination. Instead, the composition of α + δ eutectoid is ca. 35 wt% Cu and 43 wt% Sn and is relatively rich in Cl (10 wt%), O (11 wt%), and Si (1 wt%).

It's important to note that the corrosion attack from the rim to the core of the section is not uniform, and the behavior within the corroded dendrites varies depending on the exposure conditions [32].

In the inner part of the section the oxidation of only Sn from the δ phase suggests an oxygen potential high enough to oxidize Sn, but too low to oxidize Cu and to efficiently passivate the tin-rich δ phase [33]. On the contrary, near the surface of the coin section, both Sn and Cu are oxidized. Specifically, the presence of chloride ions in the burial environment and high oxygen potential favour the mechanism of cuprite corrosion and redeposition [8].

Moving from the core to the rim of the section, SEM observations of the sample unveiled two distinct layers of corrosion on the coin's surface:

- A thick, bright layer of oxides, observed in BSE mode.
- A thinner, dark external concretion layer primarily composed of copper chlorides.

The presence of cuprite appears as a blue-gray shade in bright-field microscopy (Fig. 2). In regions where tiny voids exist within the cuprite crust, nearly perfect cube-shaped crystals of this mineral protrude into the hollow spaces. Additionally, small pockets of redeposited copper are observable within the partially mineralized zone, intermingling with the residual dendrites.

The X-ray maps of Cu K (pink), Sn L (green), O K (light blue), Cl K (yellow) Si K (blue) signals are reported in Fig. 2. Chlorine is locally observed in the bulk alloy and in the outer corrosion layer. Sn is concentrated in the inter-dendritic spaces in the inner zone of the cross-section; oxygen is present in the intermediate partially mineralized zone and in the external layer, associated with silicon and chlorine. The exogenous compounds are characteristic of soil contamination.

The features of this coin suggest that the alloy was solidified without any homogenization treatment. Indeed, even dendrites show different shapes and morphologies, suggesting local variations in solidification conditions, including cooling rates and metal flow. Specifically, in the

Table 1
X-ray Microscopy (XRM) scanning parameters.

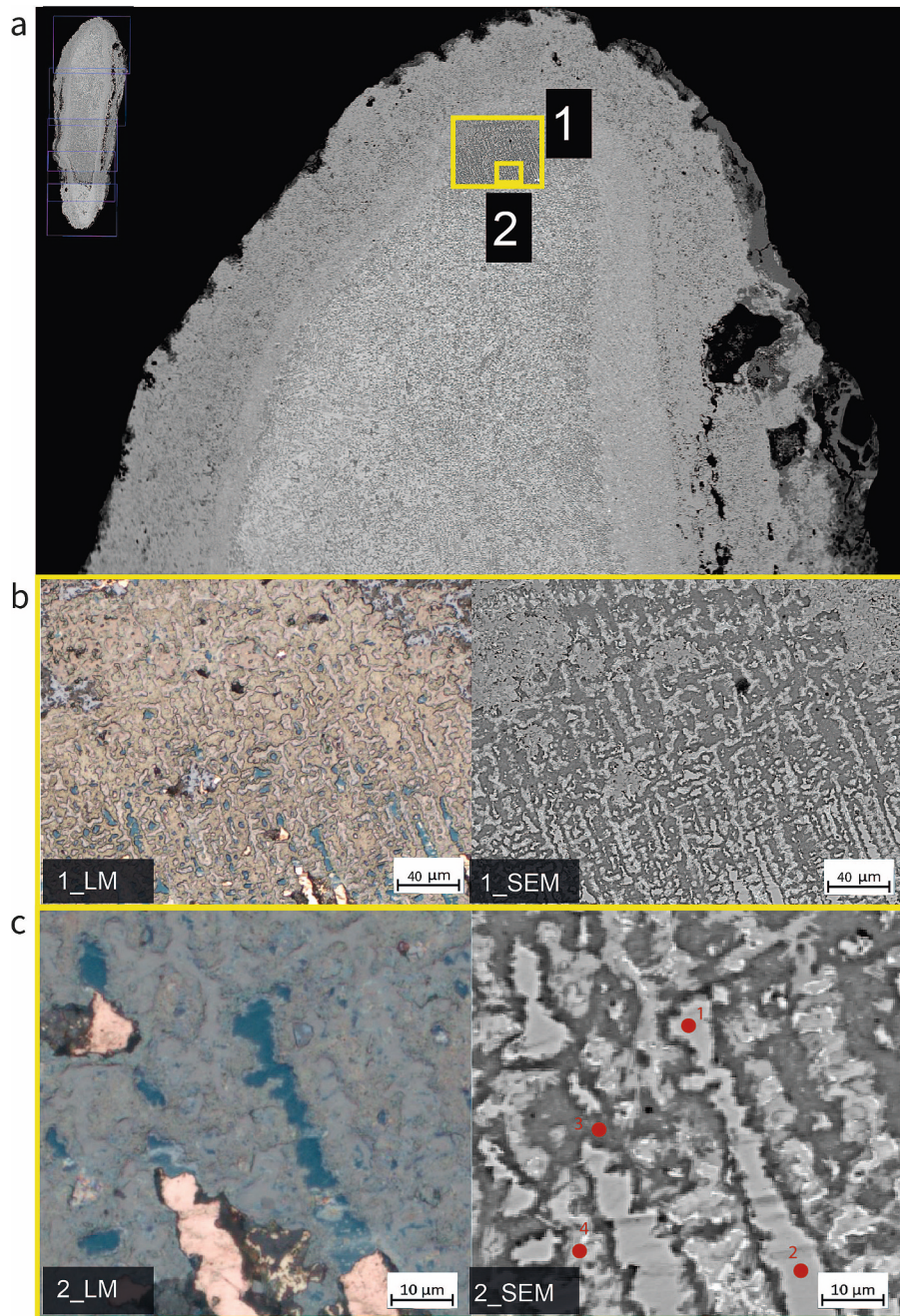| Sample	Objective	Pixel size (μm)	Voltage (kV)	Power (W)	Exposure time (s)	#projections
MO 89 BIII 43/3	0.4×	13.8	160.0	25.0	1.3	1601
	4×	3.0	160.0	25.0	7	3201
MO 89 B 40/1	0.4×	12.0	160.0	25.0	1.3	1601
	4×	2.2	160.0	25.0	5.1	3201
MO 91 B 103/6	0.4×	15.0	160.0	25.0	0.5	1601
	4×	2.7	150.0	23.0	5	3201
MO 91 B 278/2	0.4×	13.6	160.0	25.0	1.0	1601
	4×	3.3	160.0	25.0	3.6	3201

Fig. 1. Correlation of 2D imaging (LM, SEM) views of coin MO 89 BIII 43/3. (a) Location of targeted ROI for LM and SEM–EDS imaging and analysis. These were collected 'live' to enable correlation to specific areas. (b) Axio imager and SEM image of corroded dendritic microstructure. (c) Detail of corrosion in cored α-Cu dendrites (points 1,2 and 3) and in α + δ eutectoid (point 4).

Table 2
Bronze matrix points scanning analysis results of coin MO 89 BIII 43/3 (see Fig. 1).

Position	Cu (wt%)	Sn (wt%)	Cl (wt%)	O (wt%)	Si (wt%)
1	92.00	4.14	3.86	–	–
2	96.93	3.07	–	–	–
3	65.77	5.14	29.09	–	–
4	35.00	42.61	10.29	10.78	1.32

edges of the coin, the presence of elongated and narrow dendrites indicates a faster heat dissipation compared to the center. This can lead to faster cooling conditions at the edges, promoting the growth of elongated dendrites. The flow direction may have also favored the growth of elongated dendrites at the edges, where the flow is more direct, while at the center, where the flow is more isotropic, more rounded dendrites have formed [27].

CLEM revealed that coin MO 89 B 40/1 is made of three principal zones: (1) an uncorroded metal core, (2) an intermediate chlorine-rich zone, and (3) an outer completely mineralized zone (Fig. 3). The α-Cu solid solution is composed of ca. 100 wt% of Cu. The grains are small (20 μm) and flattened with the Pb segregation phases (white inclusions) along the intergranular spaces (98 wt% of Cu and 2 wt% of Sn). According to the Cu—Pb binary phase diagram, this lead-rich constituent, with a Pb content of approximately 99.9 wt%, is formed at a low temperature eutectic (326 °C). EDS chemical analyses are reported in
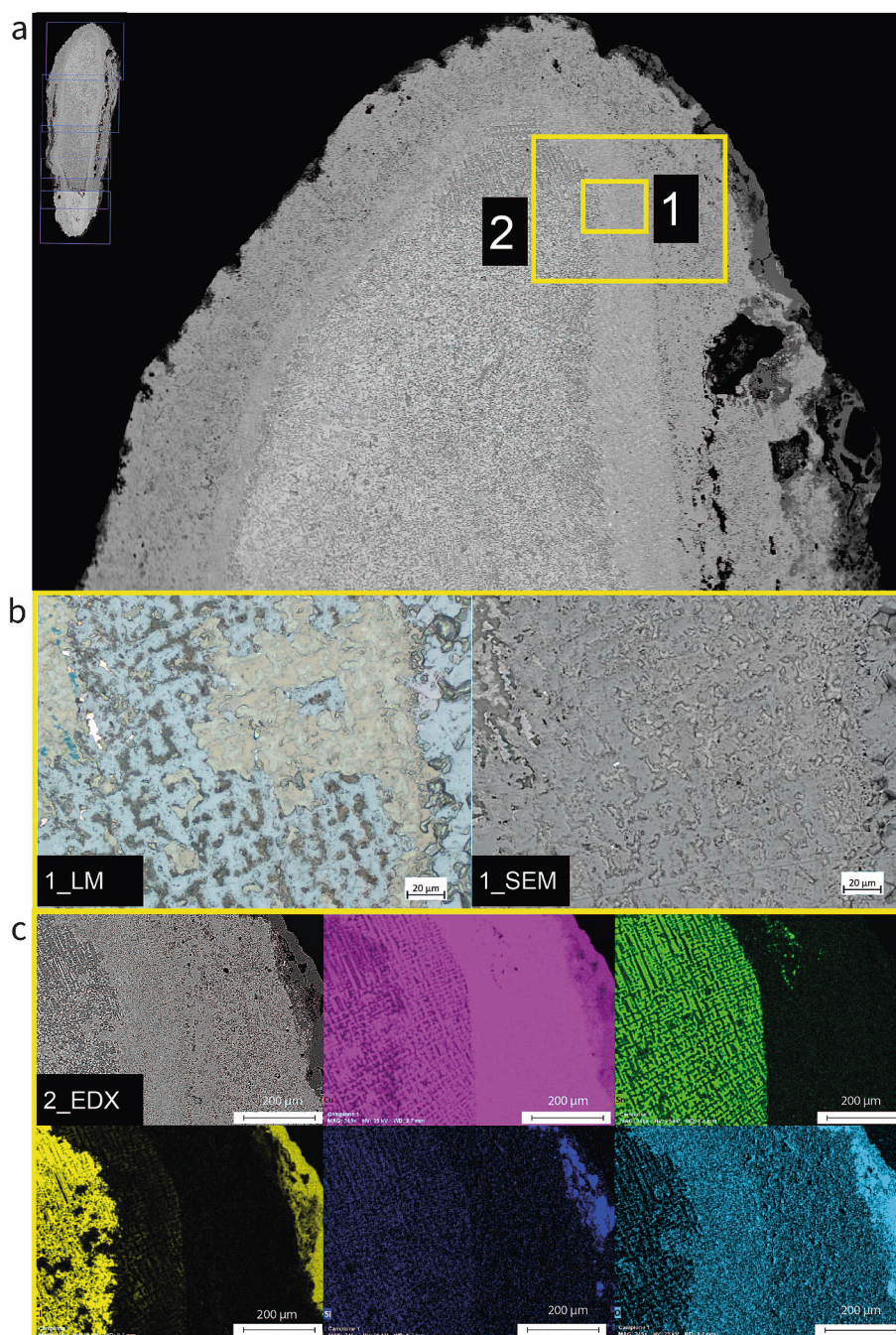
Fig. 2. Correlative LM, SEM images of coin MO 89 BIII 43/3. (a) Location of targeted ROI for LM and SEM–EDS imaging and analysis. (b) Axio imager and SEM image of redeposited cuprite. (c) SE image and X-ray maps of Cu, Sn, Cl, Si and O.

(Table 2S, **Supplementary Materials**).

As confirmed by SEM–EDS observations in Fig. 3b, the intermediate corrosion layer is primarily characterized by the presence of discontinuous and elongated copper chloride islands (63 wt% Cu, 33 wt% Cl, and 4 wt% O). These islands replace copper grains and intricately intermingle between the compact metal core and the outer layers of the coin. Atop the copper chloride species, a thin layer of lead chloride compounds forms, consisting of 63 wt% Pb, 14 wt% Cu, 18 wt% Cl, and 5 wt% O. Indeed, over time lead diffused and migrated towards the surface through the alloy porosity and the capillary channels created during the corrosion process. In this context, the lead globules react with water, oxygen, and chloride ions from the environment, serving as an anode and initiating localized pitting corrosion [34].

Fig. 3c shows that the α-Cu solid solution is uncorroded, whereas the interdendritic area with a higher Sn and Pb content is more severely corroded. At high magnifications SEM images disclose the presence of nanometer crystallites of cassiterite SnO_2 deposited mainly in little disconnected at the intergranular positions [24,35].

In Fig. 4b, EDX maps clearly show the distribution of Cl in the intragranular spaces, while Pb infiltrates the intergranular spaces towards the outer section. In Fig. 4c, it is observed the presence of inclusions of different nature in the α + δ eutectoid: Pb chloride-based inclusions and cassiterite inclusions, as previously discussed.

Coin MO B 103/6 exhibits a microstructure similar to that of coin MO 89 B 40/1 but displays a higher lead content in the outer layers and an increased tin content (Fig. 5a). In Fig. 5b, it is possible to observe the
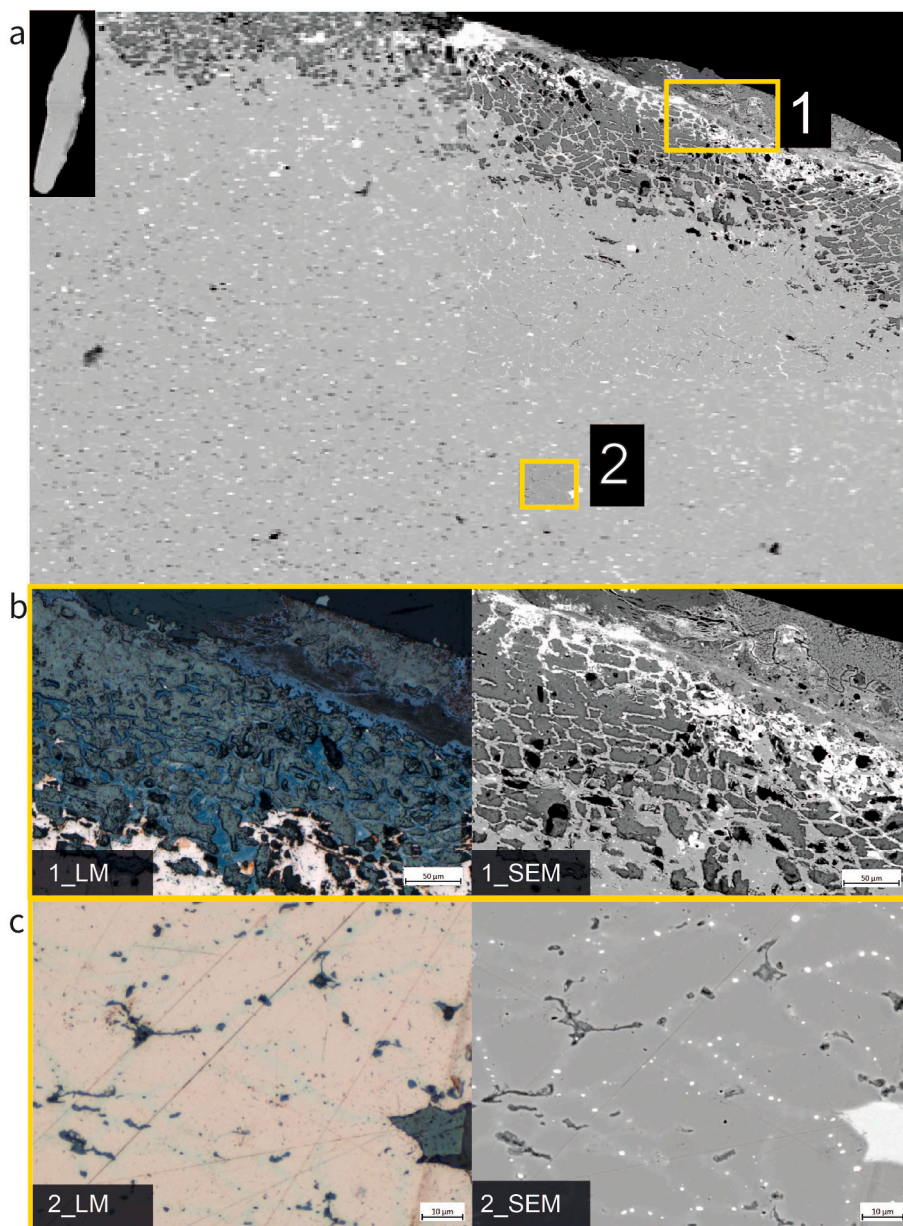
Fig. 3. CLEM views of coin MO 89 B 40/1. (a) Location of targeted ROI for LM and SEM–EDS imaging and analysis. (b) LM and SEM image of corrosion layers, showing intermediate chlorine-rich zone, and outer completely mineralized zones (c) Detail of matrix showing alpha grains with nanometer crystallites of cassiterite and Pb- segregation phases (white inclusions) along the intergranular spaces.

stratification of corrosion products on the patina. In particular, analysis with SEM on the light gray phase revealed the presence of nantokite, which is converted into hydrate copper chlorides ($Cu_2(OH)_3Cl$) in the outer dark layer. Lead occurs as white strips and lumps in the patina with the composition of 73 wt% of Pb, 10 wt% of S, 4 wt% of Cu as well as the mixture of Pb, Cu oxides, and chlorides. Fig. 5c shows a similar intermediate corrosion layer, characterized by the substitution of copper grains in copper chloride islands (61 wt% Cu, 33 wt% Cl, 3 wt% of Sn and 3 wt% O) along intergranular spaces, consisting of 64 wt% Cu, 15 wt % of Sn, 12 wt% Cl, 4 wt% O and 3 wt% of S. The inner core is composed of α-Cu grains made of 98 wt% Cu and 2 wt% Sn. Lead phases are found within the intergranular spaces, composed of 47 wt% Cu, 4 wt% Sn, 8 wt % Cl, and 40 wt% Pb (Fig. 5d).

Coin MO 91 B 278/2 has a partially dendritic microstructure, but in contrast with the other coins, this one has considerably deformed dendrites (Fig. 6). This coin is composed of α-Cu phase (98 wt% of Cu; 1 wt% of Sn; 1 wt% of Fe) and inter-dendritic spaces, occupied by 87 wt% of Cu

and 13 wt% of Sn (Fig. 6e). Along the interdendritic phases, Pb-rich microparticles are found (59 wt% of Cu, 9 wt% of Sn, and 32 wt% of Pb). In the areas where the metal is highly deformed, the dendrites are following the metal movement and deformation. Furthermore, the presence of numerous slip lines can be found in the corroded grains on the striking surface of the coin, suggesting that it was heavily worked during the minting process (Fig. 6c). EDS investigation revealed the nature of corrosion, which is propagated mainly in a transgranular direction along slip lines caused by cold deformation, resulting in higher O and Cl concentrations.

4.2. Patina analysis by μ-Raman spectroscopy

The four Phoenician–Punic bronze coins selected for this study are shown in (Table 1S, Supplementary Materials). On bronze surfaces, LM displays mainly three parts of the patina: one green patina, one light blue in colour - occurring especially in coins MO 91 B 103/6 and MO 91
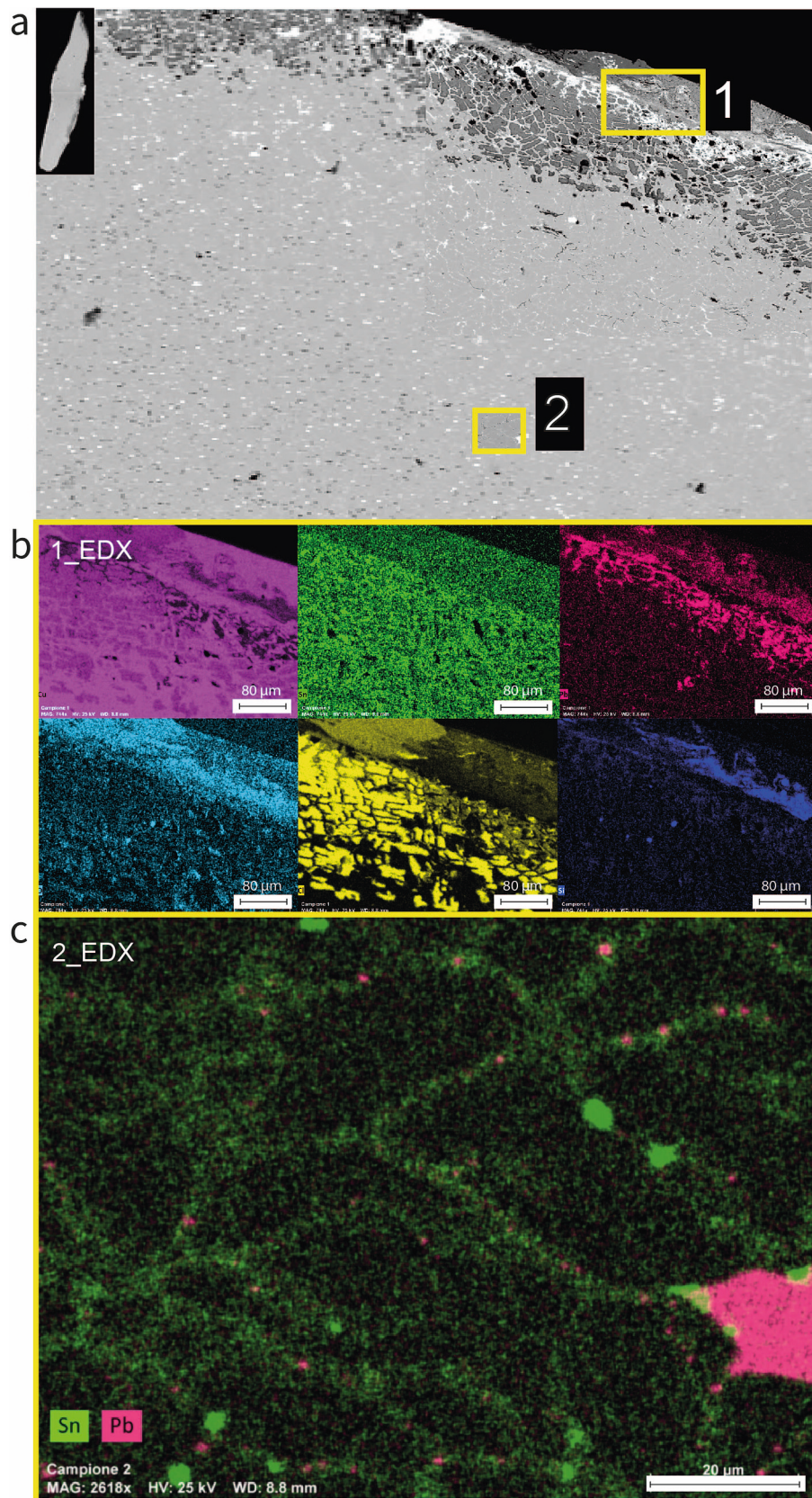
Fig. 4. CLEM views of coin MO 89 B 40/1. (a) Location of targeted ROI for EDX maps (b) EDX maps of Cu, Sn, Pb, O, Cl, and Si (c) EDX map of Sn and Pb superimposed on BSE image showing alpha grains with cassiterite inclusions and Pb- segregation phases.
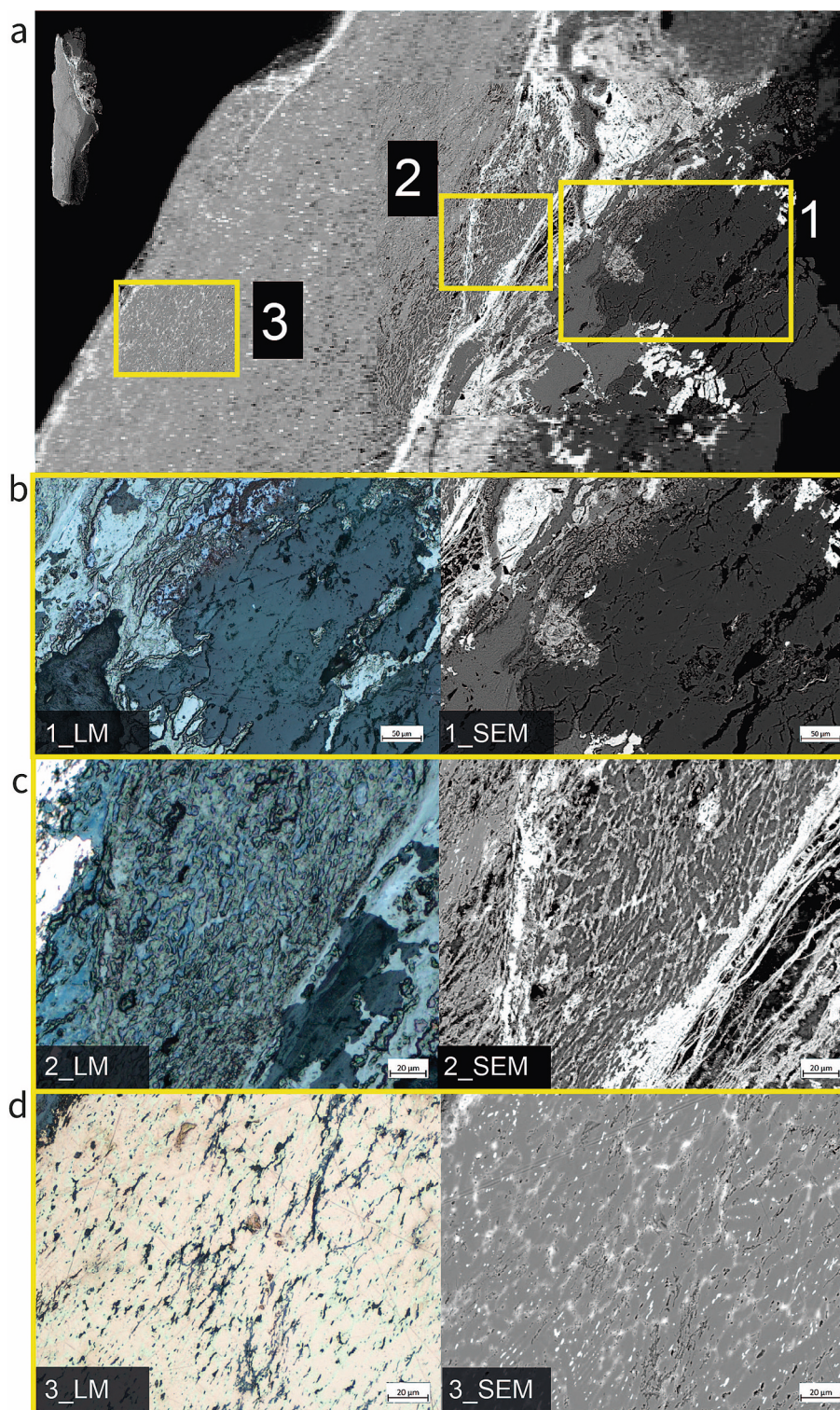
Fig. 5. CLEM views of coin MO B 103/6. (a) Location of targeted ROI for LM and SEM–EDS imaging and analysis. (b) LM and SEM detail of outer mineralized zones. (c) Detail of intermediate chlorine-rich zone and Pb-rich patina (d) Detail of inner core made of α-Cu grains and lead phases at intergranular position.

B 278/2 and representing approximately half of the total thickness in the outside range - and one red near the metal patina interface.

To determine the mineralogical composition of different corrosion compounds, the surface of the coins was analyzed using μ-Raman spectroscopy (Fig. 7, Table 3).

In unleaded bronze coins MO 89 B III 43/3 and MO 91 B 278/2, Raman analysis revealed the presence of the cuprous oxide cuprite

(Cu_2O) and the copper hydroxychlorides ($Cu_2Cl(OH)_3$), which are frequently detected on archaeological bronzes in marine environments; the first normally appearing at the interface between metal and environment and the latter occurring in conditions of high relative humidity and chloride supply.

The spectrum in Fig. 7a (coin MO 91 B 103/3) as well as the spectrum in Fig. 7b,d,e show a strong peak at 218 cm^{-1}, ascribed to the
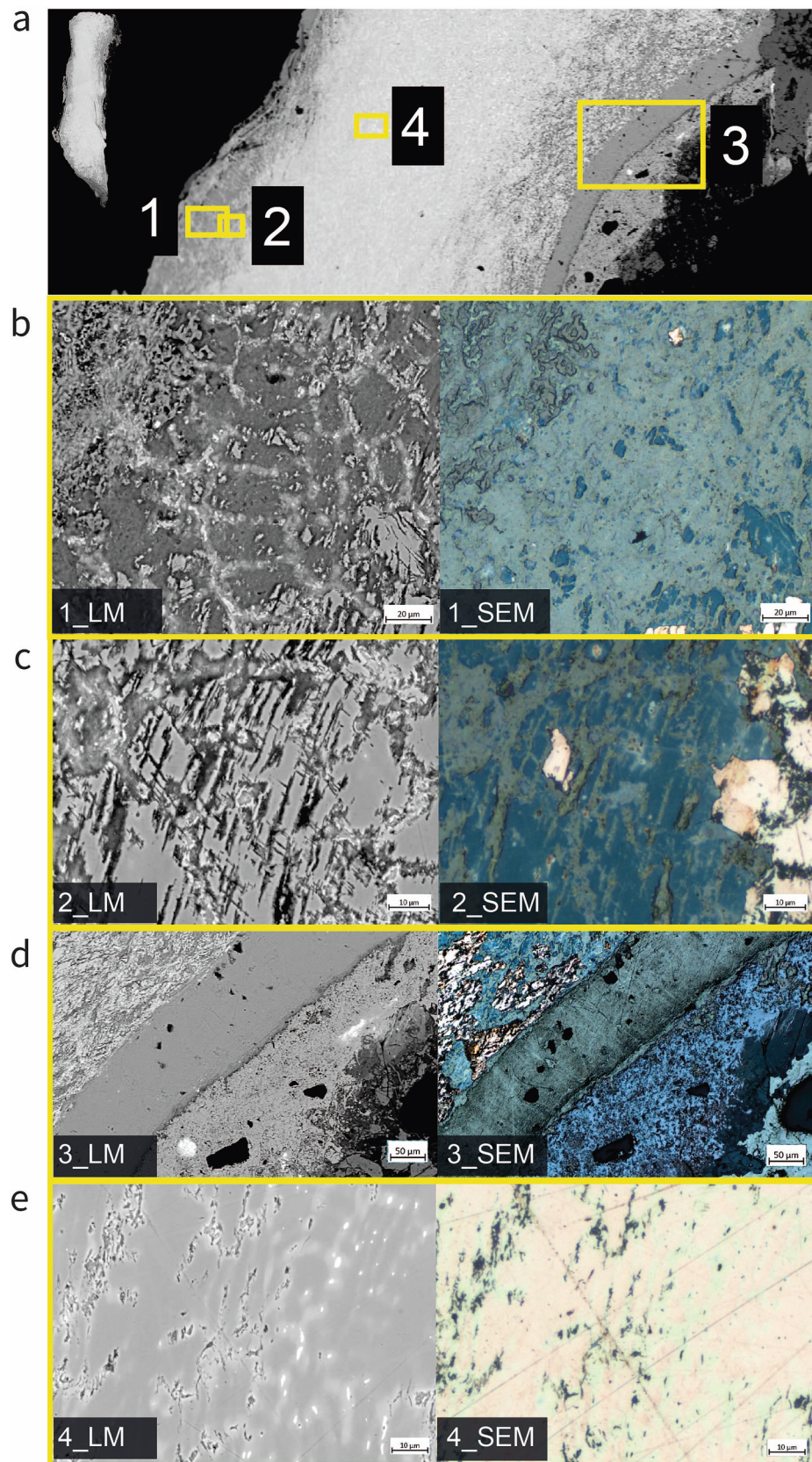
Fig. 6. CLEM views of coin MO 91 B 278/2. (a) Location of targeted ROI for LM and SEM–EDS imaging and analysis. (b) LM and SEM detail of chlorine-rich zone. (c) Detail of slip lines in corroded grains on the striking surface. (d) Copper chloride vein in the intermediate zone (e) Detail of deformed and corroded alpha grains and scarse Pb-inclusions at intergranular position.
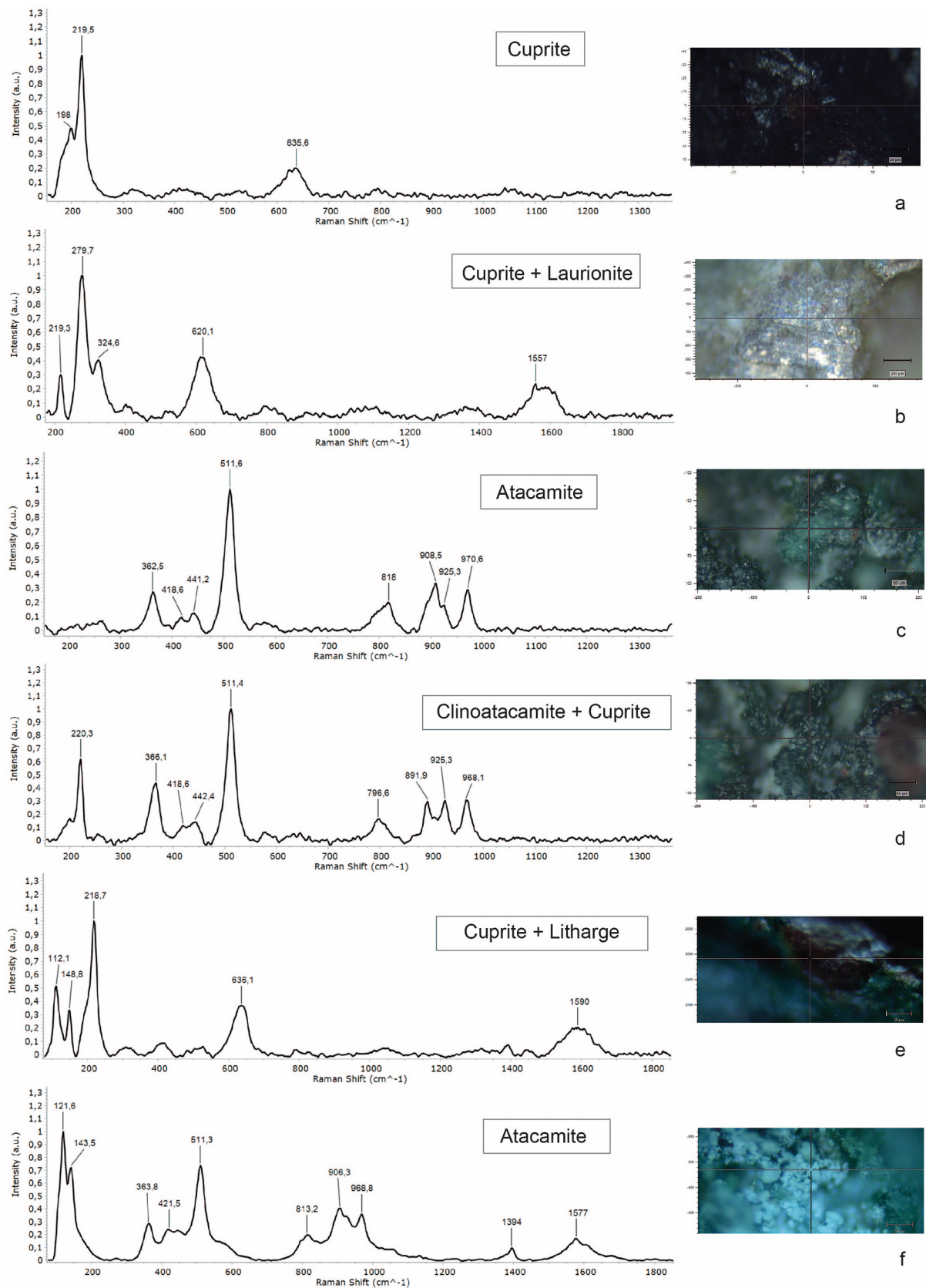
Fig. 7. Raman spectra acquired on the surface of the coins: (a) cuprite, (b) combined spectra of cuprite and laurionite, (c) atacamite, (d) combined spectra of cuprite and clinoatacamite (e) combined spectra of cuprite and litharge, (f) atacamite.

Corrosion products	MO 89 B III 43/3	MO 89 B 40/1	MO 91 B 103/6	MO 91 B 278/2
Cuprite	●●●●	●●●●	●●●●	●●
Atacamite	●●●	–	●	●●●
Clinoatacamite	●	–	–	–
Laurionite	–	●●●	–	–
Litharge	–	–	●●●	–
Calcite	–	●	–	●

characteristic vibrational mode of cuprite (Cu_2O) and broad peaks centered at ca 416 cm^{-1} and 637 cm^{-1}, that could be assigned to defective cuprite forming a native passive layer on copper/bronze objects [36–39].

Notably, copper hydroxychloride can be distinguished from other corrosion products in the medium-frequency region of the Raman spectrum, specifically associated with Cu–O–H bending modes [5]. Atacamite, a prevalent component in most coins except for MO 89 B 40/1, is characterized by Raman peaks at 818, 908, and 970 cm^{-1}(Fig. 7c,f), indicative of hydroxyl deformation [5]. Remarkably, in the low––medium wavenumber region, the spectrum of atacamite exhibits a subtle shift towards higher wavelengths (362 cm^{-1}) compared to the typical atacamite (approximately 354 cm^{-1}). This shift is attributed to the emerging formation of clinoatacamite, the ultimate polymorph in the series and considered the most stable according to Ostwald's law. Specifically, on the surface of coin MO 89 B III 43/3, clinoatacamite shows a higher degree of crystallization, evident from discernible peaks at 796, 891, and 968 cm^{-1}(Fig. 7d). The unstable nantokite (CuCl) phase is not found as a corrosion product because it forms only under dry environmental conditions.

The absence of tin corrosion products detected with micro-Raman spectroscopy on the surface of corroded bronzes of type 2 can be explained by the nanometric size and poor crystallization of hydrated tin (IV) oxides, making them difficult to identify with this technique, as highlighted by studies indicating these oxides' tendency to form amorphous phases [40,41].

In leaded bronze alloys, as it was the case on MO 89 B 40/1, MO 91 B 103/6, PbO oxides (i.e., litharge) and chlorides (i.e., laurionite) are encountered in the patina. In coin MO 91 B 103/6 it forms a thin protective layer of lead oxide (litharge α-PbO), identified by the two strong peaks at 112 and 148 cm^{-1} and broad peaks at 311 and 415 cm^{-1}, in combination with cuprite, recognized by peaks at 218 cm^{-1} (Fig. 7e).

Coin MO 89 B 40/1 is characterized by a significant amount of laurionite (PbCl(OH)), detected at 279, 324, 620 cm^{-1} [42] (Fig. 7b). The presence of the lead chloride-containing compound as a corrosion product indicates the presence of dissolved chloride anions in the burial soil. The percolation of saline water to the burial soil causes the formation of lead chloride and oxychloride minerals.

The $(CO_3)^{2-}$ group of carbonates is characterized by a strong band at around 1081 cm^{-1} due to the symmetric stretching vibration and at 710 cm^{-1} due to the plane bending mode of the carbonate groups. This is attributed to the presence of calcite ($CaCO_3$) in the soil.

4.3. 3D multi-scale imaging of coins for casting technique

XRM results offered a detailed representation of the internal features and hidden details of the samples. We utilized XRM datasets initially to identify the cross-section of each coin for CLEM investigation. Subsequently, these datasets were used to contextualize analytical and microscopic information in three dimensions, providing precise insights into the evolution of corrosion microstructures in concealed areas of the object.

XRM reconstructed datasets were analyzed slice-by-slice along the X,

Y, and Z directions to get insights about the overall distribution of different phases and their corrosion products within the samples. The XRM data obtained from coin MO 89 BIII 43/3 are summarized in Fig. 8.

The obverse, center and reverse sides of the coin MO 89 BIII 43/3 are compared through XRM investigations and reported in Fig. 8a. The greyscale levels displayed in XRM images represent portions of the sample characterized by different densities. Notably, when examining the image on the right, we can reconstruct the relief that depicts a horse, which had been obscured by the layers of corrosion on the coin. Observing the slices near the center of the coin and those at the edges in Fig. 8b, we discern the propagation of the stratified structure and selective corrosion from the core to the surface. This structure reveals the arrangement of the main phases, highlighting a corroded core primarily composed of Cu—Sn (gray), which corresponds to the dendritic microstructure described in the previous paragraphs. On this core, we observe a denser layer (bright area) showing a Cu-enriched region, recognized as redeposited cuprite. In the outer layers, fully mineralized phases are detected, mainly composed of copper chlorides.

In Fig. 8b, on the right side of the coin, specifically at the edge, we readily identify an area with a higher concentration of a metallic phase, appearing as a brighter region. These phases correspond to a non-corroded α-Cu solid solution. This distinctive feature could be attributed to variations in the coin's exposure to a chloride-containing environment. XRM, even at low- resolution scans, allowed to detect losses and discontinuities in the external corrosion layers and internal breakage planes within the coin not visible from the outside. A similar corrosion pattern was observed in a bronze needle originating from the same archaeological context in Motya [24], which exhibited complete dealloying.

Since we were interested in gaining three-dimensional information at higher resolution from specific volumes of interest (VOIs), we located them within the sample using the *Scout-and-Zoom* procedure. To assess the relative volumes of the different phases inside the coin, we performed a histogram-based thresholding segmentation on a high-resolution XRM scan. This method allows to mark and label groups of pixels, according to their greyscale values, which can then be investigated separately (Fig. 8c). Each phase was compared to a reference volume, representing the entire object, to obtain its volumetric fraction. The calculated volume of the dendritic corroded core (yellow) consists of 41 % of the total coin volume, Cu-rich zone (pink) represents the 38 % of the volume, the crack (magenta) contributes for the 3 % to the whole sample and the remaining 18 % is related to a dark external concretion layer (blue), which corresponds to volumetric regions with an increased Cl-content. These percentages should be viewed as qualitative indicators meant to provide a general sense of the trends and patterns observed, rather than exact numerical accuracy.

Coin MO 89 B 40/1 exhibits a compact and homogeneous core throughout its volume (Fig. 9a, b). The presence of a circular high-density area, indicating a Pb lump, on the obverse side of the coin, corresponds to the horse's chest. Moreover, a brighter edge is noticeable, stemming from the existence of a thin lead-rich patina and micrometric lead inclusions scattered along the edges of the coin [43], as confirmed by previous chemical/elemental investigations. The distribution of Pb along the edges of the coin (depicted in green) becomes distinctly apparent when performing an histogram-based thresholding segmentation (Fig. 9c). It reveals that this element is dispersed along the boundaries and appears as corrosion byproducts on the surface of the coin, occupying totally only 2 % of the total volume of the coin.

Based on the XRM observations conducted on coin MO 91 B 103/6, the coin exhibits severe corrosion, fragmentation, and notable variations in thickness and density within its corrosion layers (refer to Fig. 10a,b). Notably, the corrosion layers are so substantial in this instance that they hinder the clear identification of the coin type. The presence of lead is particularly concentrated in the outer part of the coin, forming a discernibly thick layer that is visible as green patches (see Fig. 10c). This lead-rich layer occupies a substantial 11 % of the total volume of the
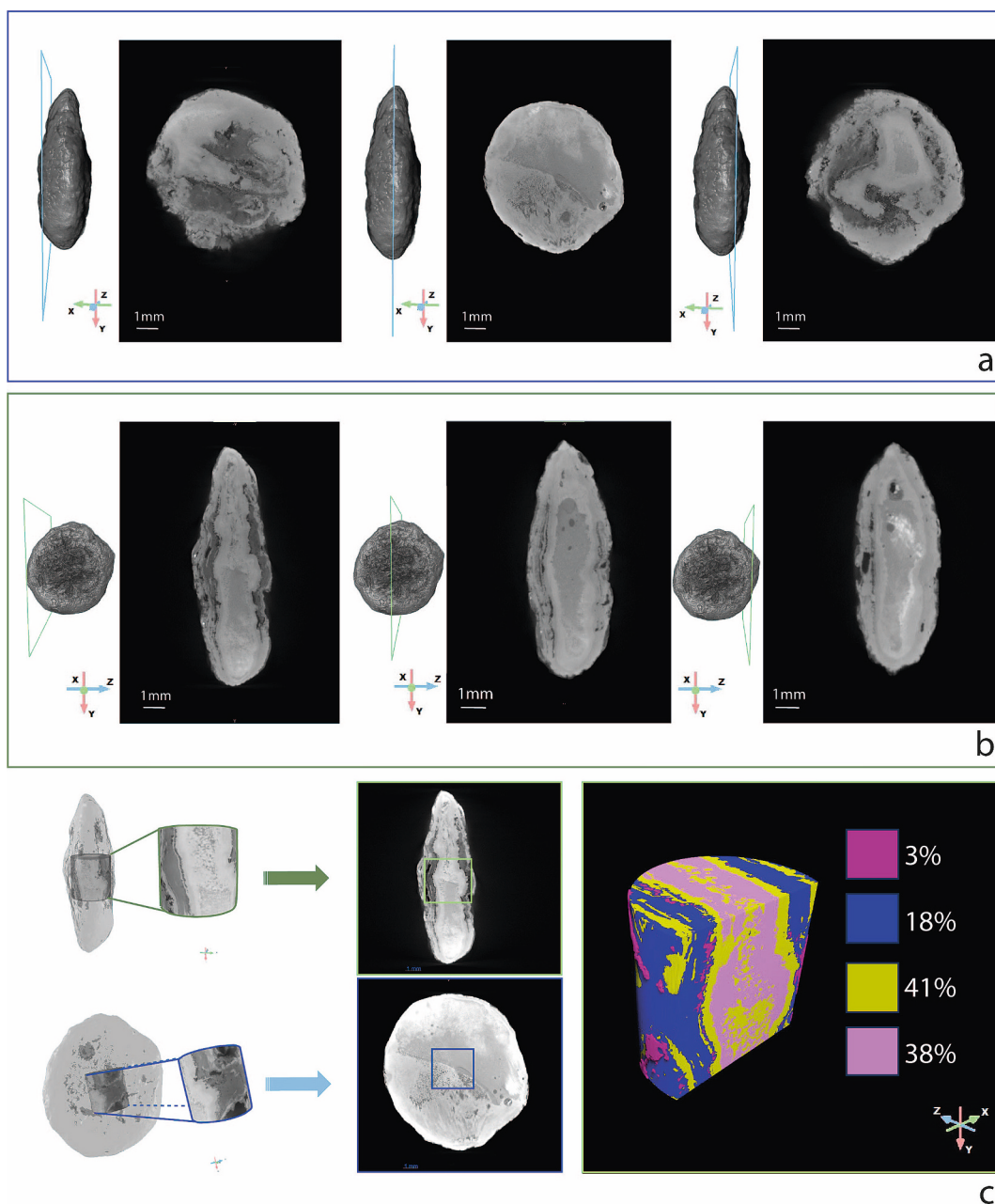
Fig. 8. X-ray microscopy slices illustrating coin MO 89 B III 43/3 microstructure acquired at different positions. (a) three virtual cross-sections parallel to the faces of the coins. (b) three virtual slices perpendicular to the face of the coins. (c) 3D rendering of ROI analyzed in detail via high-resolution XRM and segmentation of different layers with relative percentage composition: magenta—cracks, blue—Cl-rich layer, yellow—corroded core, pink —Sn— poor zone. (For interpretation of the references to colour in this figure legend, the reader is referred to the web version of this article.)

coin.

Coin MO 91 B 278/2 is characterized by an extensive incrustation of greenish corrosion products, which appear black in XRM imaging, not adhering to the coin's surface, as shown in Fig. 11a,b. Upon conducting higher-resolution XRM scans of a selected volume of the coin (Fig. 11c), we noticed the presence of a texture similar to a dendritic structure, as detailed in the previous paragraphs. In particular, a high-resolution scan enables us to discern both the primary and secondary arms of dendrites. This suggests that the cooling rate was relatively rapid, as evidenced by the formation of small dendrites.

In this context, as shown in Fig. 11c, the presence of Pb in the alloy in this case is negligible and it is concentrated in the outer layers of corrosion in the form of microscopic globules. This information is significant because it suggests that lead is not a deliberate addition to the alloy, but it could be the result of environmental factors influencing the surface of the coin over time.

5. Discussion

The present study underscores the critical importance of combining various analytical methods in a multiscale and multimodal correlative microscopy environment to gain a comprehensive understanding of metallurgical processes and material properties (the complete correlative microscopy workflow can be seen in Video 1). One of the key advantages of correlative microscopy is its ability to acquire, connect and analyze various data types simultaneously, offering a comprehensive view of the subject. This holistic approach is invaluable when examining historical coinage and minting techniques.
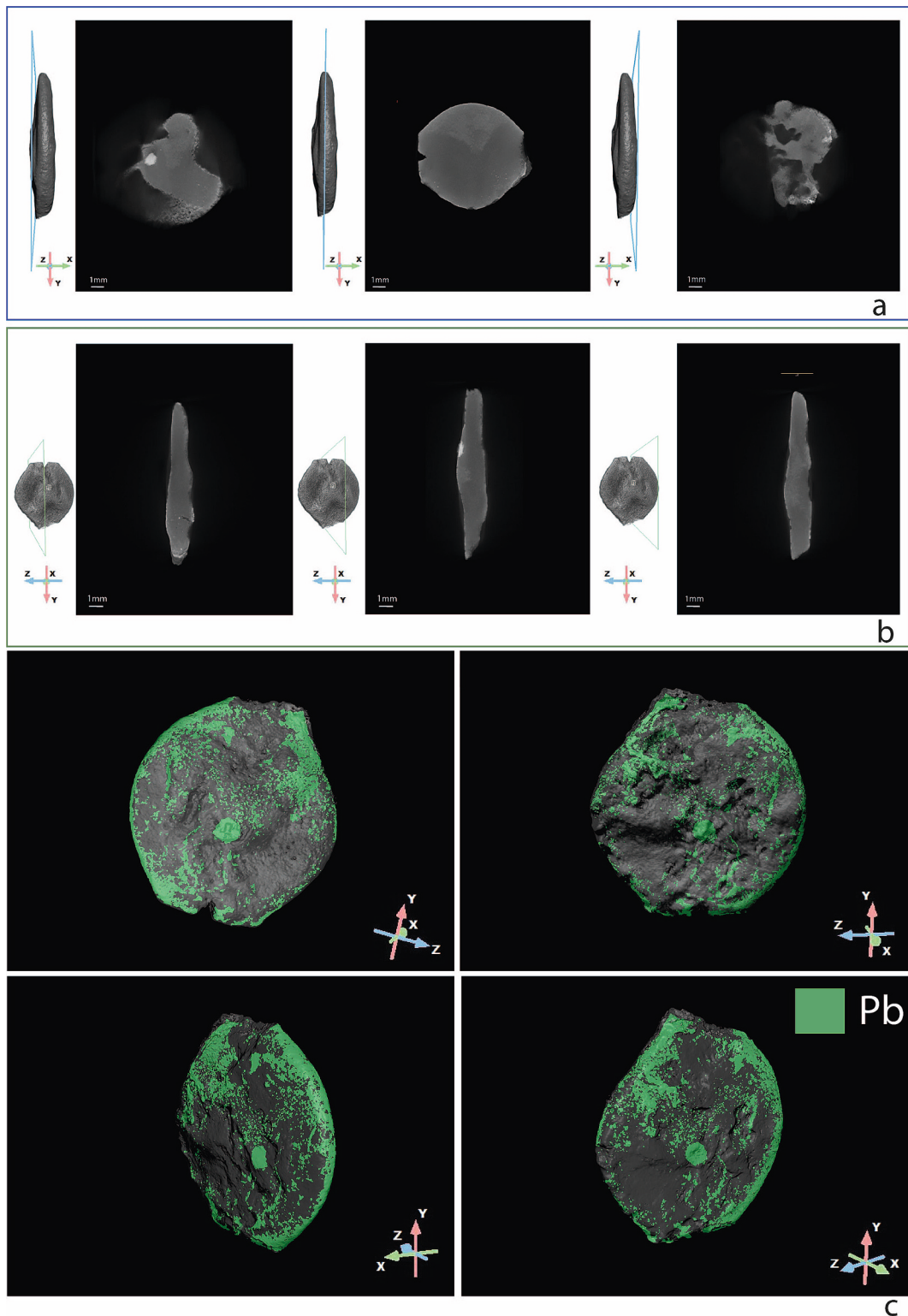
Fig. 9. X-ray microscopy slices illustrating coin MO 89 B 40/1 microstructure acquired at different positions. (a) three virtual cross-sections parallel to the faces of the coins. (b) three virtual slices perpendicular to the face of the coins. (c) segmentation of Pb-phases representing ca. 2 % of the coin.

From CLEM metallographic examination of coin MO 89 BIII 43/3 by LM and SEM it was possible to determine that this coin is composed of binary alloy in an advanced state of corrosion. Indeed, the section of the coin nearest the surface suffered a massive attack on the alpha phase by chlorine, leaving only fragmented remnants of the metal dendrites. However, further into the core of the section, the dendritic eutectoid has been preferentially corroded, whereas the alpha phases remain in a good

state of conservation, as can be seen readily in Fig. 12a. This result is in accordance with [28], which demonstrates that the corrosion rate in the interdendritic segregation area is significantly higher than that in the dendrite area. This study reported the microarea potential on the microstructure of antique cast low Sn bronze in a chlorine-containing environment. They found that the surface potential of the segregation site is significantly lower than that of the dendritic site, indicating a
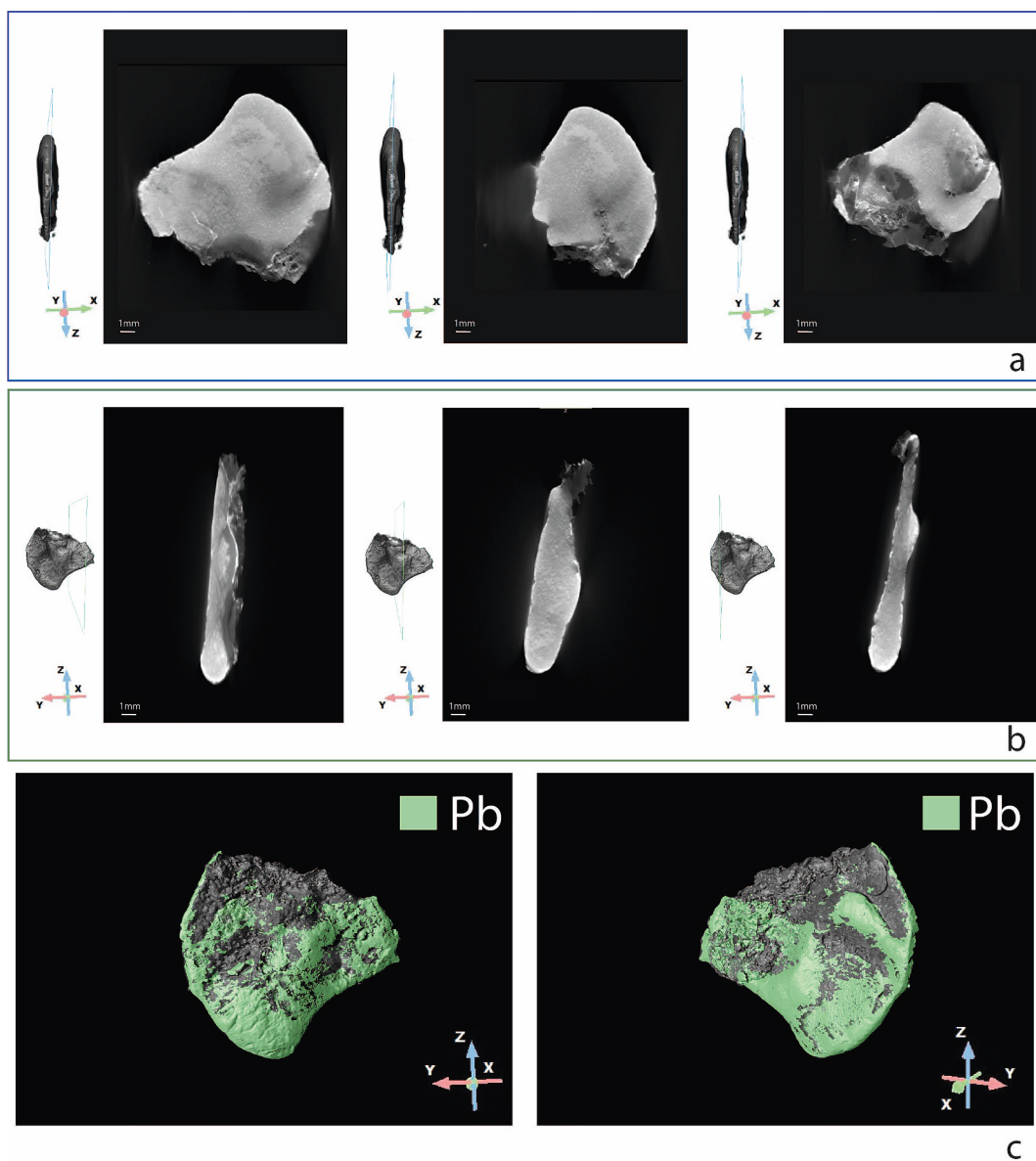
Fig. 10. X-ray microscopy slices illustrating coin MO 91 B 103/6 microstructure acquired at different positions. (a) three virtual cross-sections parallel to the faces of the coins. (b) three virtual slices perpendicular to the face of the coins. (c) segmentation of Pb-phases representing ca. 11 % of the coin.

lower thermodynamic stability. Indeed, Gibbs's free energy is influenced by the surface potential. This implies that a lower surface potential corresponds to negative Gibbs free energy, resulting in a higher corrosion tendency [28]. The network distribution of such potential differences can initiate corrosion and accelerate localized corrosion. This mechanism could explain why α + δ is preferentially corroded in the presence of chloride ions in the burial environment.

In the external layers only mineral corrosion products are found. The first is a porous and spongy phase which was recognized as redeposited cuprite. Patches of redeposited cuprite also occurred along the length of the section at the interdendritic position.

The abundance of copper trihydroxychlorides in the outer layers suggests that soil water salt may have been the primary corroding agent, leading to "bronze disease." This phenomenon essentially involves the oxidation and hydrolysis of cuprous chloride to basic cupric chloride in humid weather [43].

$$4CuCl + O_2 + 4H_2O \rightarrow 2Cu_2(OH)_3Cl + 2H^+ + Cl^- \qquad \Delta(G^0)_f$$

$$= -360.9 kJ/mol$$
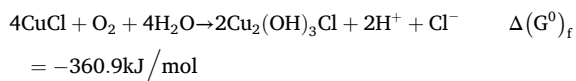
Based on the μ-Raman spectroscopy results, it can be inferred that coin MO 89 B III 43/3 is in a more advanced stage of corrosion, as the sequence of polymorphs is nearing completion and the system has reached equilibrium. Conversely, the other coins exhibit an ongoing corrosion process. For instance, corrosion products like atacamite change their crystalline structure over time, leading to an increase in their volume and contributing to the rapid degradation of the artifact.

In contrast to coin MO 89 BIII 43/3, no dendrites are detected in the other coins (MO 89 B 40/1, MO 91 B 103/6, MO 91 B 278/2), which are characterized by flattened and deformed α grains, which are sure signs of a cold worked annealed metal. The leaded bronzes have a primary alpha phase with an alpha plus delta eutectoid as well as lead inclusions distributed in granular form at the interdendritic positions of Sn segregation. As shown in Fig. 12b, the darker gray areas represent tin-rich phases, and the medium gray regions are copper-rich. From these features, it is possible to determine that this coin was cold-work hardened after casting and subsequently stroked. Regarding the corrosion products formed on the surface of the bronze alloy, on coin MO 89 B 40/1, the major corrosion products were cuprite (Cu_2O) and laurionite (PbCl
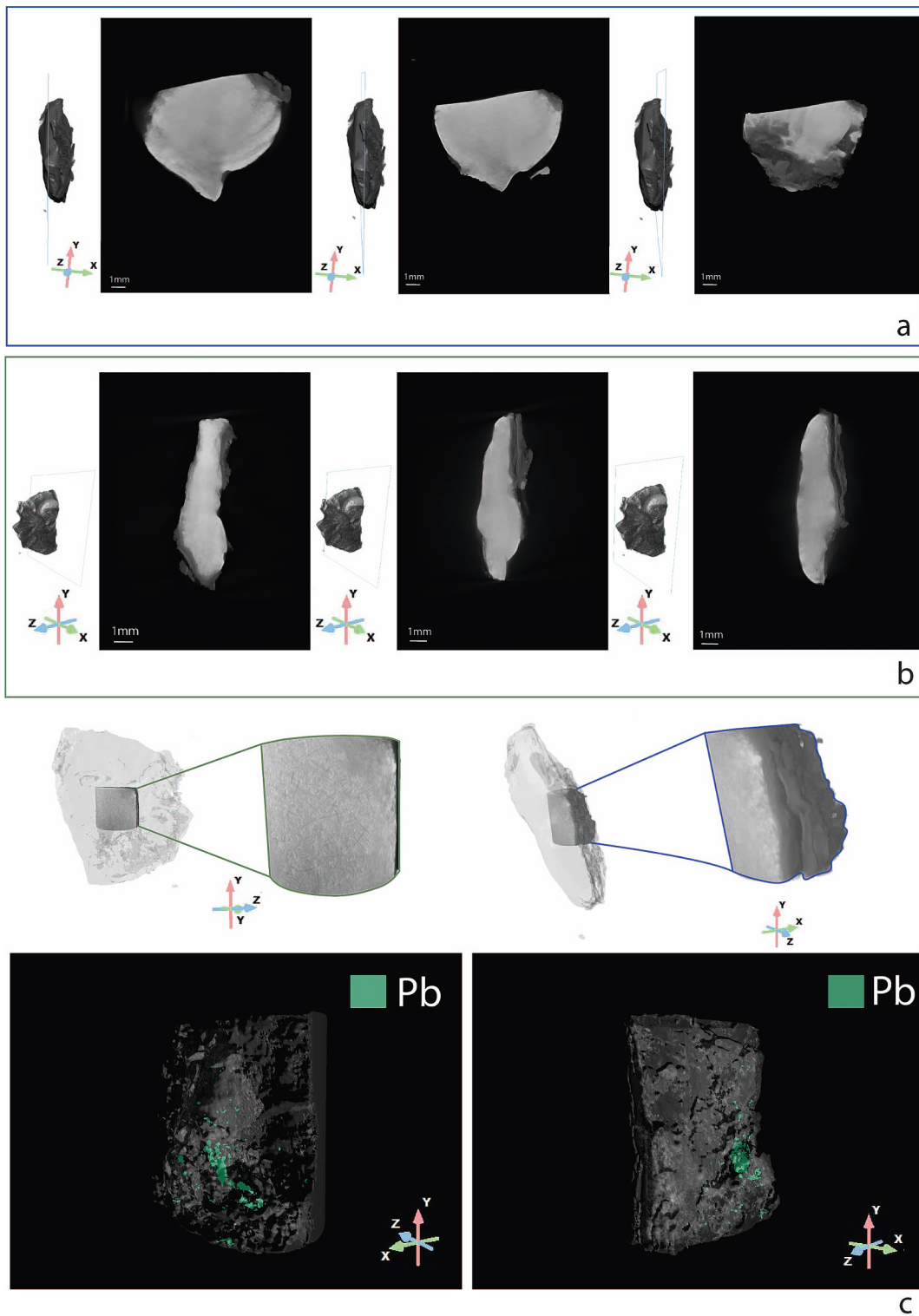
Fig. 11. XRM slices illustrating coin MO 91 B 278/2 microstructure acquired at different positions. (a) three virtual cross-sections parallel to the faces of the coins. (b) three virtual slices perpendicular to the face of the coins. (c) 3D rendering of ROI analyzed in detail via high-resolution XRM and segmentation of Pb-phases in the ROI.

(OH)). In particular, laurionite PbCl(OH) is formed when the pH of the natural saline environment (*i.e.*, chloride concentration is about 0.5 M and pH is about 8) is increased, matching with the lagoon-like environment of Motya [44–46].

$$2PbO + H_2O + 2Cl^- \rightarrow 2Pb(OH)Cl$$
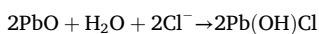
The corrosion products in the coin MO 91 B 103/6 consisted principally of Cu_2O and litharge (α-PbO). The formation of this phase depends on the conditions of cooling, the grain dimensions, and the form and the degree of perfection of crystallites formed under high temperatures. This product, which is the most thermodynamically stable polymorph at ambient temperature, is obtained at slow cooling.
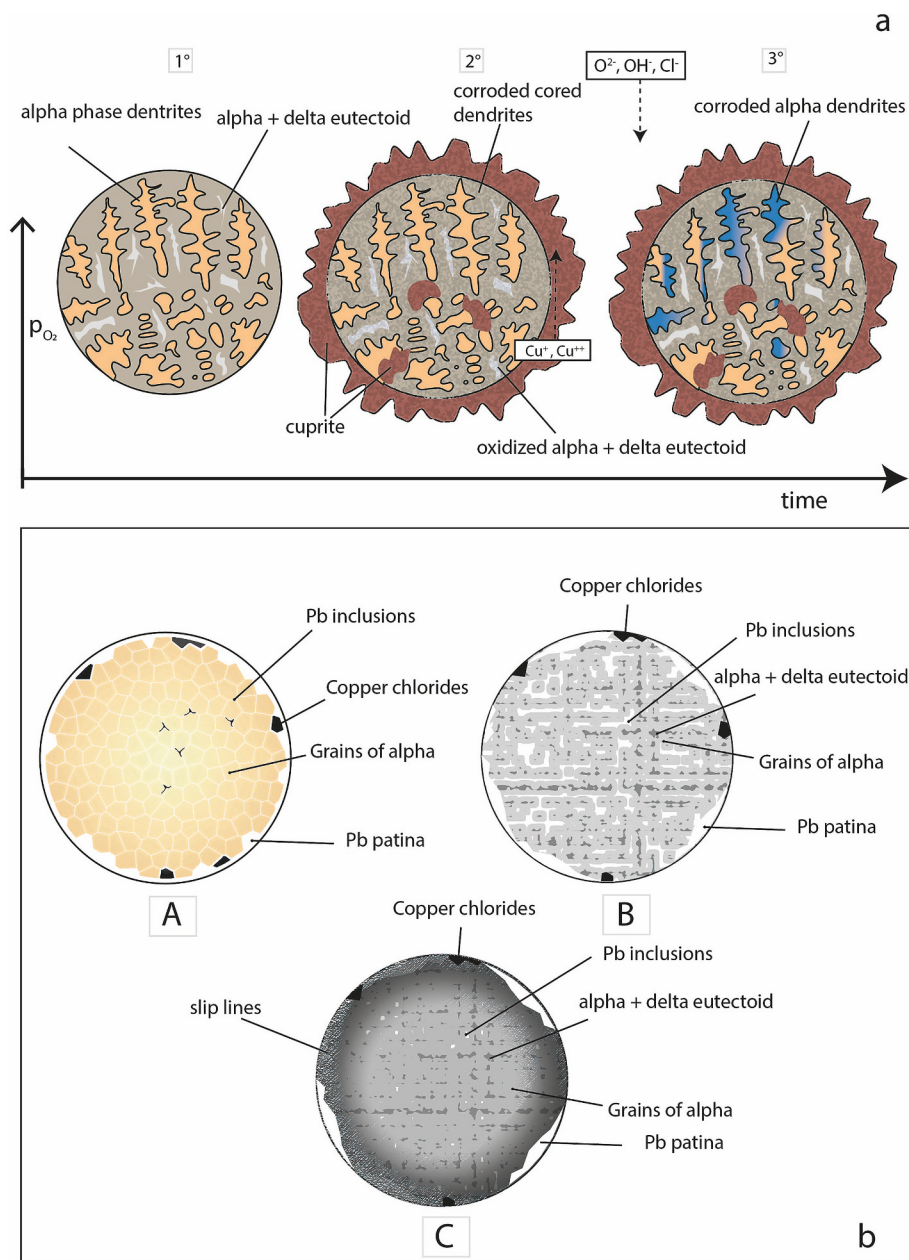
$$Pb + 1/2\ O_2 \rightarrow PbO\ (\text{litharge})$$
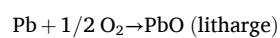
Fig. 12. Schematic corrosion models of low-Sn bronze coins in Cl-containing environment. (a) corrosion evolution in coin MO 89 BIII 43/3. (b) corrosion pattern of coins MO 89 B 40/1(A), MO 91 B 103/6 (B), MO 91 B 278/2 (C).

Conversely, a more rapid cooling tends to preserve the other polymorph, massicot β-PbO [47]. However, the mixture of corrosion products could be attributed to various environmental conditions that affected the object in the burial context and storage area.

XRM extends to characterizing Phoenician archaeological coins by revealing internal features and hidden sample details. It enables us to estimate and analyze irregularities such as cracks and pits on the surface and inside the coins, as well as examine the phase composition in three dimensions without compromising the integrity of the analyzed material. Indeed, XRM operates in a non-invasive manner, allowing for the distinction of phases without the need for sampling. Leveraging previously analyzed chemical compositions, XRM further enables the estimation of volumetric percentages for each phase. For instance, the higher concentration of a metallic phase on one side of the coin MO 89 BIII 43/3 could be attributed to variations in the coin's exposure to a chloride-containing environment. It is conceivable that the coin may have been vertically buried in the soil, resulting in differential corrosion rates between its two sides. Consequently, as the corrosion progressed, there was an escalation in corrosion depth within this segregated area. This, in turn, led to an accelerated corrosion rate, eventually causing the transformation of the metallic core into corrosion products. XRM data also provided valuable insights into the type of casting, the amount of lead, and its distribution within the alloy. Indeed, the morphology and distribution of lead phases offer valuable insights into the casting methods employed in antiquity, particularly whether they were employed for vertical or horizontal techniques. In the vertical casting method, a series of standing blanks was crafted within a sealed mold by pouring molten alloy from above. Conversely, the horizontal casting method was utilized to create horizontally positioned blanks, utilizing either open or sealed molds [14]. In this case, the concentration of Pb at the ends of the coin MO 89 B 40/1 is a proof of the vertical technique, whereas the more uniform dispersion of Pb in coin MO 91 B 103/6 indicates a potential employment of a horizontal casting technique in the coin's production. Furthermore, the use of XRM has facilitated a detailed

study of the reliefs on ancient coins covered with corrosion layers, revealing the presence of a horse obscured by the layers of corrosion on the coin MO 89 BIII 43/3.

6. Conclusion

The main conclusions can be summarized in the following key points:

- The integrated approach of CLEM, μ-Raman spectroscopy and XRM has proven to be essential in gaining a comprehensive view of ancient coins, allowing the examination of internal structure, metal composition, and corrosion processes.
- Each coin displayed distinctive features in its structure and composition, unveiling diverse as-cast microstructures characterized by varying shapes and morphologies of dendritic patterns. These variations were dependent on the concentration of Sn in the alloy and the level of work hardening. Notably, coin MO 91 B 278/2 exhibited numerous slip lines, indicating significant working during the minting process.
- CLEM analysis provided details about corrosive phases and differentiated corrosion processes in various microstructures of the coins. In particular, it can be inferred that coin MO 89 B III 43/3 is in a more advanced stage of corrosion, as it suffered a massive attack by chlorine, leaving only fragmented remnants of the metal dendrites. The study also confirmed that the interdendritic segregation area is the first to corrode compared to the dendrite area.
- μ-Raman spectroscopy allowed the study of mineralized phases, providing information about the kinetics and environmental conditions governing the formation of copper hydroxychloride, i.e., clinoatacamite and atacamite and lead salts, i.e., lead oxides and laurionite on the patina of the coins.
- The use of XRM enabled the three-dimensional reconstruction of coins, highlighting stratifications, corrosion areas and visualization of previously obscured reliefs on coins surface. Additionally, this method allowed for the quantification of lead inclusions in each coin, reaching 11.47 % of the total volume in the case of coin MO 91 B 103/6.

In conclusion, this work not only deepens our understanding of the examined ancient coins but also emphasizes the importance of an integrated approach in addressing complex issues related to metallurgy and the conservation of historical artifacts. The application of advanced techniques offers new perspectives in the field of archaeology and heritage conservation, with significant implications for understanding the interactions between metallic materials and corrosive environments over time.

Supplementary data to this article can be found online at https://doi.org/10.1016/j.matchar.2024.114441.

CRediT authorship contribution statement

Martina Bernabale: Writing – review & editing, Writing – original draft, Visualization, Methodology, Investigation, Formal analysis, Conceptualization. **Flavio Cognigni:** Writing – review & editing, Writing – original draft, Visualization, Methodology, Investigation, Formal analysis, Conceptualization. **Silvia Contessi:** Writing – review & editing, Investigation. **Anacleto Proietti:** Writing – review & editing, Investigation. **Chiara Mancini:** Writing – review & editing, Investigation. **Federica Spagnoli:** Writing – review & editing, Resources, Funding acquisition. **Marco Rossi:** Supervision, Resources, Funding acquisition. **Caterina De Vito:** Writing – review & editing, Supervision, Funding acquisition.

Declaration of competing interest

The authors declare that they have no known competing financial interests or personal relationships that could have appeared to influence the work reported in this paper.

Data availability

Data will be made available on request.

References

[1] T.H. Rehren, E. Pernicka, Coins, artefacts and isotopes-archaeometallurgy and archaeometry, Archaeometry 50 (2008) 232–248, https://doi.org/10.1111/j.1475-4754.2008.00389.x.

[2] M. Di Fazio, F. Di Turo, L. Medeghini, L. Fabrizi, F. Catalli, C. De Vito, New insights on medieval Provisini silver coins by a combination of non-destructive and micro-invasive techniques, Microchem. J. 144 (2019) 309–318, https://doi.org/10.1016/j.microc.2018.09.016.

[3] M.T. Doménech-Carbó, F. Di Turo, N. Montoya, F. Catalli, A. Doménech-Carbó, C. De Vito, FIB-FESEM and EMPA results on Antoninianus silver coins for manufacturing and corrosion processes, Sci. Rep. 8 (2018) 1–12, https://doi.org/10.1038/s41598-018-28990-x.

[4] F. Di Turo, N. Montoya, J. Piquero-Cilla, C. De Vito, F. Coletti, G. Favero, A. Doménech-Carbó, Archaeometric analysis of Roman bronze coins from the magna mater temple using solid-state voltammetry and electrochemical impedance spectroscopy, Anal. Chim. Acta 955 (2017) 36–47, https://doi.org/10.1016/j.aca.2016.12.007.

[5] G. Bertolotti, D. Bersani, P.P. Lottici, M. Alesiani, T. Malcherek, Micro-Raman Study of Copper Hydroxychlorides and Other Corrosion Products of Bronze Samples Mimicking Archaeological Coins, 2012, pp. 1451–1457, https://doi.org/10.1007/s00216-011-5268-9.

[6] F. Di Turo, F. Coletti, C. De Vito, Investigations on alloy-burial environment interaction of archaeological bronze coins, Microchem. J. 157 (2020) 104882, https://doi.org/10.1016/j.microc.2020.104882.

[7] L. Fabrizi, F. Di Turo, L. Medeghini, M. Di Fazio, F. Catalli, C. De Vito, The application of non-destructive techniques for the study of corrosion patinas of ten Roman silver coins: the case of the medieval Grosso Romanino, Microchem. J. 145 (2019) 419–427, https://doi.org/10.1016/j.microc.2018.10.056.

[8] G.M. Ingo, L.I. Manfredi, G. Bultrini, E. Piccolo, Quantitative analysis of copper-tin bronzes by means of glow discharge optical emission spectrometry, Archaeometry 39 (1) (1997) 59–70, https://doi.org/10.1111/j.1475-4754.1997.tb00790.x.

[9] T. De Caro, E. Angelini, L. Es Sebar, Application of μ-Raman spectroscopy to the study of the corrosion products of archaeological coins, Acta Imeko 10 (2021) 234, https://doi.org/10.21014/acta_imeko.v10i1.893.

[10] G.M. Ingo, T. De Caro, C. Riccucci, E. Angelini, S. Grassini, S. Balbi, P. Bernardini, D. Salvi, L. Bousselmi, A. Çilingiroğlu, M. Gener, V.K. Gouda, O.A.L. Jarrah, S. Khosroff, Z. Mahdjoub, Z.A.L. Saad, W. El-Saddik, P. Vassiliou, Large scale investigation of chemical composition, structure and corrosion mechanism of bronze archeological artefacts from Mediterranean basin, Appl. Phys. A Mater. Sci. Process. 83 (2006) 513–520, https://doi.org/10.1007/s00339-006-3550-z.

[11] F. Di Turo, Limits and perspectives of archaeometric analysis of archaeological metals: a focus on the electrochemistry for studying ancient bronze coins, J. Cult. Herit. 43 (2020) 271–281, https://doi.org/10.1016/j.culher.2019.10.006.

[12] B. Bakirov, I. Saprykina, S. Kichanov, R. Mimokhod, N. Sudarev, D. Kozlenko, Phase composition and its spatial distribution in antique copper coins: neutron tomography and diffraction studies, J. Imaging 7 (2021), https://doi.org/10.3390/jimaging7080129.

[13] S.E. Kichanov, K.M. Nazarov, D.P. Kozlenko, I.A. Saprykina, E.V. Lukin, B. N. Savenko, Analysis of the internal structure of ancient copper coins by neutron tomography, J. Surf. Invest. 11 (2017) 585–589, https://doi.org/10.1134/S1027451017030296.

[14] M. Griesser, W. Kockelmann, K. Hradil, R. Traum, New insights into the manufacturing technique and corrosion of high leaded antique bronze coins, Microchem. J. 126 (2016) 181–193, https://doi.org/10.1016/j.microc.2015.12.002.

[15] S.E. Nagler, A.D. Stoica, G.M. Stoica, K. An, H.D. Skorpenske, O. Rios, D.B. Hendin, N.W. Bower, Time-of-flight neutron diffraction (TOF-ND) analyses of the composition and minting of ancient judaean "biblical" coins, J. Anal. Methods Chem. 2019 (2019), https://doi.org/10.1155/2019/6164058.

[16] F. Cognigni, M. Rossi, H. Stegmann, G. Sciuto, G. Anastasi, M. Astuto, M. Bonadonna, D. Mello, A multiscale and multimodal correlative microscopy workflow to characterize copper segregations identified in epitaxial layer of power MOSFETs, in: ISTFA, ASM International, 2023, pp. 92–100, https://doi.org/10.31399/asm.cp.istfa2023p0092.

[17] F. Cognigni, M.E.E. Temporiti, L. Nicola, N. Gueninchault, S. Tosi, M. Rossi, Exploring the infiltrative and degradative ability of fusarium oxysporum on polyethylene terephthalate (PET) using correlative microscopy and deep learning, Sci. Rep. 13 (1) (2023) 22987, https://doi.org/10.1038/s41598-023-50199-w.

[18] F. Cognigni, L. Miraglia, S. Contessi, F. Biancardi, M. Rossi, Correlative light and Electron microscopy (CLEM): a multifaceted tool for the study of geological specimens, J. Exp. Theor. Anal. 1 (2) (2023) 74–85, https://doi.org/10.3390/jeta1020006.

[19] F. Giuntoli, L. Menegon, G. Siron, F. Cognigni, H. Leroux, R. Compagnoni, M. Rossi, A.V. Brovarone, Methane-hydrogen-rich fluid migration may trigger seismic failure in subduction zones at forearc depths, Nat. Commun. 15 (1) (2024) 480, https://doi.org/10.1038/s41467-023-44641-w.

[20] R. White, S. Kelly, Correlative, multi-scale, lab-based X-ray tomography: from millimeters to nanometers, Microsc. Microanal. 26 (2020) 2020–2021, https://doi.org/10.1017/S1431927620016621.

[21] R.L. Mitchell, P. Davies, P. Kenrick, T. Volkenandt, C. Pleydell-Pearce, R. Johnston, Correlative microscopy: a tool for understanding soil weathering in modern analogues of early terrestrial biospheres, Sci. Rep. 11 (2021) 1–14, https://doi.org/10.1038/s41598-021-92184-1.

[22] M. Bernabale, F. Cognigni, L. Nigro, M. Rossi, T. De Caro, C. De Vito, A comprehensive strategy for exploring corrosion in iron - based artefacts through advanced multiscale X - ray microscopy, Sci. Rep. (2022) 1–9, https://doi.org/10.1038/s41598-022-10151-w.

[23] T. Chang, A. Maltseva, P. Volovitch, I. Odnevall Wallinder, C. Leygraf, A mechanistic study of stratified patina evolution on Sn-bronze in chloride-rich atmospheres, Corros. Sci. 166 (2020) 108477, https://doi.org/10.1016/j.corsci.2020.108477.

[24] D. Šatović, L.V. Žulj, V. Desnica, S. Fazinić, S. Martinez, Corrosion evaluation and surface characterization of the corrosion product layer formed on cu-6Sn bronze in aqueous Na2SO4 solution, Corros. Sci. 51 (2009) 1596–1603, https://doi.org/10.1016/j.corsci.2009.04.002.

[25] D.A. Scott, Metallography and Microstructure in Ancient and Historic Metals, Getty Publications, 1992.

[26] X. Wang, J. Song, H. Zhou, Z. Fan, J. Shi, J. Chen, K. Xiao, Mechanism of dendrite segregation on corrosion behaviour of antique cast low Sn bronze, Corros. Sci. 222 (2023) 111402, https://doi.org/10.1016/j.corsci.2023.111402.

[27] M. Bernabale, F. Cognigni, C. Mancini, A. Proietti, F. Mura, D. Montanari, L. Nigro, M. Rossi, C. De Vito, 3D fractures analysis and conservation assessment of wrought iron javelin through advanced non - invasive techniques, Sci. Rep. (2023) 1–11, https://doi.org/10.1038/s41598-023-37179-w.

[28] M. Bernabale, F. Cognigni, F. Mura, L. Nigro, D. Montanari, M. Rossi, C. De Vito, 3D imaging of micro-segregation and corrosion behavior of alloying elements in archaeological artefacts from Motya (Sicily, Italy), Corros. Sci. 211 (2023) 110900, https://doi.org/10.1016/j.corsci.2022.110900.

[29] L.I. Manfredi, La Monetazione Punica in Sicilia, Sardegna e Italia Meridionale : venti anni di Studi, C, 2018, pp. 867–887.

[30] P.I.A. Proposito, D. Elusiva, A. Campana, Motya : Litra Con Testa di Ninfa e Offerente, 2014, pp. 3–27.

[31] S. Frey-Kupper, Coins and Their Use in the Punic Mediterranean: Case Studies From Carthage to Italy From the Fourth to the First Century BCE, 2014, https://doi.org/10.1017/CBO9781107295193.008.

[32] G. Masi, J. Esvan, C. Josse, C. Chiavari, E. Bernardi, C. Martini, M.C. Bignozzi, N. Gartner, T. Kosec, L. Robbiola, Characterization of typical patinas simulating bronze corrosion in outdoor conditions, Mater. Chem. Phys. 200 (2017) 308–321, https://doi.org/10.1016/j.matchemphys.2017.07.091.

[33] A.S. Saraiva, E. Figueiredo, H. Águas, R.J.C. Silva, Characterisation of archaeological high-tin bronze corrosion structures, Stud. Conserv. 0 (2020) 1–15, https://doi.org/10.1080/00393630.2020.1857523.

[34] M. Bernabale, L. Nigro, D. Montanari, A.M. Niveau-de-villedary, C. De Vito, Microstructure and chemical composition of a Sardinian bronze axe of the Iron Age from Motya (Sicily, Italy), Mater. Charact. 158 (2019), https://doi.org/10.1016/j.matchar.2019.109957.

[35] A. Petitmangin, I. Guillot, A. Chabas, S. Nowak, M. Saheb, S.C. Alfaro, C. Blanc, C. Fourdrin, P. Ausset, The complex atmospheric corrosion of α/δ bronze bells in a marine environment, J. Cult. Herit. 52 (2021) 153–163, https://doi.org/10.1016/j.culher.2021.09.011.

[36] V. Bongiorno, S. Campodonico, R. Caffara, P. Piccardo, M.M. Carnasciali, Micro-Raman spectroscopy for the characterization of artistic patinas produced on copper-based alloys, J. Raman Spectrosc. 43 (2012) 1617–1622, https://doi.org/10.1002/jrs.4167.

[37] M. Serghini-idrissi, M.C. Bernard, F.Z. Harrif, S. Joiret, K. Rahmouni, A. Srhiri, H. Takenouti, V. Vivier, M. Ziani, Electrochemical and Spectroscopic Characterizations of Patinas Formed on an Archaeological Bronze Coin 50, 2005, pp. 4699–4709, https://doi.org/10.1016/j.electacta.2005.01.050.

[38] E. Basso, C. Invernizzi, M. Malagodi, M.F. La Russa, D. Bersani, P.P. Lottici, Characterization of colorants and opacifiers in roman glass mosaic tesserae through spectroscopic and spectrometric techniques, J. Raman Spectrosc. 45 (2014) 238–245, https://doi.org/10.1002/jrs.4449.

[39] N. Montoya, E. Montagna, Y. Lee, M.T. Doménech-Carbó, A. Doménech-Carbó, Raman spectroscopy characterization of 10-cash productions from the late Chinese emperors to the republic, J. Raman Spectrosc. 48 (2017) 1337–1345, https://doi.org/10.1002/jrs.5218.

[40] P. Piccardo, B. Mille, L. Robbiola, Tin and copper oxides in corroded archaeological bronzes, Corros. Metall. Heritage Artefacts (2007) 239–262, https://doi.org/10.1533/9781845693015.239.

[41] O. Oudbashi, R. Naseri, P. Asadi Hasanvand, Long-term corrosion of copper alloys in the soil: new aspects of corrosion morphology in archaeological vessels from South-Western Iran, Herit. Sci. 12 (2024) 73, https://doi.org/10.1186/s40494-024-01176-7.

[42] A. Ross, Raman spectroscopy of selected copper minerals of significance in corrosion, Spectrochim. Acta Part A Mol. Biomol. Spectrosc. 59 (2003) 1195–1204.

[43] Z. Liang, K. Jiang, T. An Zhang, Corrosion behaviour of lead bronze from the Western Zhou dynasty in an archaeological-soil medium, Corros. Sci. 191 (2021) 109721, https://doi.org/10.1016/j.corsci.2021.109721.

[44] M. Bernabale, L. Nigro, C. Vaccaro, M. Nicoli, D. Montanari, P. Bigini, C. De Vito, Micro-Raman spectroscopy and complementary techniques for the study of iron weapons from Motya and Lilybaeum (Sicily, Italy): corrosion patterns in lagoon-like and calcarenitic hypogea environments, J. Raman Spectrosc. (2021) 272–287, https://doi.org/10.1002/jrs.6285.

[45] M. Bernabale, F. Cognigni, L. Nigro, M. Rossi, C. De Vito, Conventional and advanced techniques for archaeological diagnostic of iron artefacts, in: 2022 IMEKO TC-4 International Conference on Metrology for Archaeology and Cultural Heritage University of Calabria, Cosenza, 2022, https://doi.org/10.21014/tc4-ARC-2022.096.

[46] A.N. Abu-Baker, The corrosion characteristics and electrochemical conservation treatment for an archaeological lead ossuary from Jordan, Ge-Conservacion 22 (2022) 154–161, https://doi.org/10.37558/GEC.V22I1.1093.

[47] M. Bouchard, D.C. Smith, Catalogue of 45 reference Raman spectra of minerals concerning research in art history or archaeology, especially on corroded metals and coloured glass, Spectrochim. Acta Part A Mol. Biomol. Spectrosc. 59 (2003) 2247–2266, https://doi.org/10.1016/S1386-1425(03)00069-6.